Spectrochimica Acta Part A: Molecular and Biomolecular Spectroscopy 305 (2024) 123485

Contents lists available at ScienceDirect

Spectrochimica Acta Part A:
Molecular and Biomolecular Spectroscopy

journal homepage: www.journals.elsevier.com/spectrochimica-acta-part-a-molecular-and-biomolecular-spectroscopy

Effective fully polarizable QM/MM approaches to compute Raman and Raman Optical Activity spectra in aqueous solution

Chiara Sepali, Piero Lafiosca, Sara Gómez, Tommaso Giovannini, Chiara Cappelli *

Scuola Normale Superiore, Piazza dei Cavalieri, 7, Pisa, 56126, Italy

HIGHLIGHTS

- QM/MM with Fluctuating Charges/ Dipoles for Raman/ROA spectra in solvated systems.
- Exploring solute-solvent interactions in Raman and ROA spectra of aqueous solutions.
- Description of hydrogen bonding interactions, and the dynamical aspects of solvation.

GRAPHICAL ABSTRACT

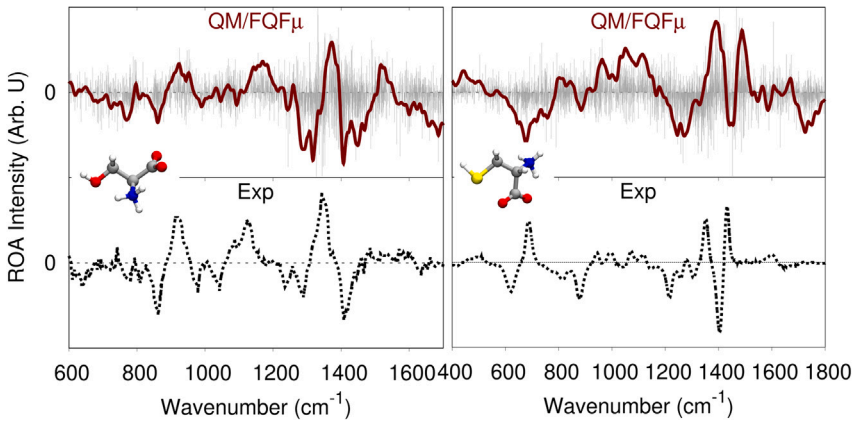

ARTICLE INFO

Keywords:
QM/MM
Hydrogen bonding
Molecular dynamics
Raman
ROA
Solvent effects

ABSTRACT

Raman and Raman Optical Activity (ROA) signals are amply affected by solvent effects, especially in the presence of strongly solute–solvent interactions such as Hydrogen Bonding (HB). In this work, we extend the fully atomistic polarizable Quantum Mechanics/Molecular Mechanics approach, based on the Fluctuating Charges and Fluctuating Dipoles force field to the calculation of Raman and ROA spectra. Such an approach is able to accurately describe specific HB interactions, by also accounting for anisotropic contributions due to the inclusion of fluctuating dipoles. To highlight the potentiality of the novel approach, Raman and ROA spectra of L-Serine and L-Cysteine dissolved in aqueous solution are computed and compared both with alternative theoretical approaches and experimental measurements.

1. Introduction

The determination of the absolute configuration of chiral molecules is central to diverse topics of study in chemistry, especially pharmaceutics and medicinal chemistry. A family of non-invasive analytical techniques has been developed in this context, all based on the differential response to polarized light, which is of the opposite sign for any pair of enantiomers [1–3]. Raman Optical Activity (ROA), which can be seen as the chiral analogous of Raman scattering [4,5], offers vibrational structure-sensitivity, and has successfully been exploited to assign the absolute configuration [6,7]. ROA was pioneered by Barron and Buckingham in 1971 [4], following the description of Rayleigh scattering of left and right circularly polarized light by chiral molecules [5]. ROA theoretical postulation was rapidly followed by the first experimental measurements [8,9]. A big boost for ROA spectroscopy was given by the development of the first commercially available instrumentation

* Corresponding author.
E-mail address: chiara.cappelli@sns.it (C. Cappelli).

https://doi.org/10.1016/j.saa.2023.123485
Received 23 June 2023; Received in revised form 22 September 2023; Accepted 1 October 2023
Available online 5 October 2023

[10,11], finally allowing ROA to be applied to a wide range of molecules and systems, with unprecedented accuracy [12–15].

Since the 2000s, ROA has been applied to a wide range of chemical systems [16–19], including not only small molecules [20], but especially proteins [10,21,22], nucleic acids, and nucleic acid–protein complexes [21,23]. The unambiguous assignment of ROA spectra to enantiomers strongly benefits from the interplay of experiment and theory [10,20–29]. However, this requires reliable approaches to predict the spectroscopic signals in a computationally viable manner [26,30,31], which cannot neglect the presence of the environment, due to its relevant, sometimes crucial, role for a correct assignment of the absolute configuration [24,25,27–29,32–34].

Multiscale Quantum Mechanical (QM)/Classical approaches [2,35–39] and in particular those accounting for the mutual polarization between the QM and MM layers [25,40–43], have shown to reliably model ROA spectra, substantially overcoming the well-known limitations of continuum solvation approaches in describing specific and directional interactions, such as hydrogen bonding [25,39,41]. To the best of our knowledge, the only polarizable QM/MM currently able to calculate ROA spectra is the QM/Fluctuating Charges (FQ) model [25,29,34,40,44], based on the Polarizable Fluctuating Charges (FQ) Force Field [45–47], which has recently been extended to several molecular properties and spectroscopies by some of the present authors [48–59]. FQ assigns each atom of the MM portion with a charge which adjusts to the potential produced by the QM region and the other MM atoms [29]. Previous studies that exploited the polarizable QM/FQ method have demonstrated the fundamental role played by mutual solute–solvent polarization in chiroptical properties and spectroscopies [25,40,44]. In addition, our recent works have shown that the inclusion of directional, anisotropic interactions allows for a better physico-chemical description of solvent effects on absorption spectra of dyes which can establish strong HBs with the surrounding water molecules [60–62]. In this work, our aim is to simulate chiral properties as ROA, thus refining the anisotropic component will enhance the physical description of certain interactions that can impact the spectroscopic signals [63]. In the FQ force field, the anisotropy of specific interactions such as HBs is indirectly obtained by positioning a fluctuating charge on each MM atom. To refine the description of the anisotropic component and consequently increase the accuracy of the solvation model, a novel polarizable force field has recently been proposed, i.e. Fluctuating Charges and Fluctuating Dipoles (FQFμ), which includes an additional polarization source described in terms of a set of fluctuating dipoles placed at the MM atoms.

In this work, QM/FQFμ is extended for the first time to the calculation of Raman and ROA spectroscopies to quantify the effects of anisotropic solute–solvent interactions. To correctly take into account conformational freedom and solvation dynamics, we exploit a well–established procedure for the simulation of spectral signals in aqueous solution, based on the coupling of QM/FQFμ with Molecular Dynamics (MD) simulations, that in order to sample the solute–solvent phase space [25,40,44]. In this way, the large sensitivity to conformational changes (especially true for ROA) and the influence of the environment on spectral signals are recovered.

As case studies, (L)-serine (SER) and L-Cysteine (CYS) are considered. SER and CYS are taken as representative amino acids, which are the molecular building blocks of peptides and play a key role in protein folding. The study of their conformational preferences is thus particularly relevant to gain insight into their H-bonding patterns [64–68]. Also, amino acids are the simplest prototypes of biomolecular systems, and thus water is their natural environment [68,69]. CYS, a precursor in food, pharmaceutical, and personal-care industries, has been previously studied both theoretically and experimentally [70–74]. Similarly to other amino acids, CYS exists as a zwitterion and its side chain stabilizes hydrophobic interactions. The presence of a hydrophilic side group in SER dramatically alters its hydrogen bonding capabilities. Hence, it has been reported that its spectra measured in water completely differ from those of other amino acids [75,76]. Finally, due to their moderate size, SER and CYS constitute suitable showcases to deeply investigate solvent effects on the Raman and ROA spectra, and to validate our computational approach. For the sake of completeness, QM/FQFμ results are compared with QM/FQ, non-polarizable QM/MM (electrostatic embedding – EE) calculations, and the implicit QM/COSMO approach [77]. The performance of all methods is also analyzed in light of their quality at reproducing experimental spectra.

2. Methods

QM/MM approaches partition a chemical system into two layers: a target (i.e. the solute in case of solvated systems), which is treated at the QM level, and an outer layer (i.e. the solvent), which is treated with classical mechanics. The system's total energy E consequently reads as follows [40]:

$$E = E_{\mathrm{QM}} + E_{\mathrm{MM}} + E^{\mathrm{int}}_{\mathrm{QM/MM}} \tag{1}$$

where E_{QM} and E_{MM} are energies of the QM and MM layers, and $E^{\mathrm{int}}_{\mathrm{QM/MM}}$ is the QM/MM interaction energy. In the specific case of polarizable embedding approaches, $E^{\mathrm{int}}_{\mathrm{QM/MM}}$ is expressed as follows [40]:

$$E^{\mathrm{int}}_{\mathrm{QM/MM}} = E^{\mathrm{ele}}_{\mathrm{QM/MM}} + E^{\mathrm{pol}}_{\mathrm{QM/MM}} + E^{\mathrm{vdw}}_{\mathrm{QM/MM}} \tag{2}$$

$E^{\mathrm{ele}}_{\mathrm{QM/MM}}$ and $E^{\mathrm{pol}}_{\mathrm{QM/MM}}$ are the electrostatic and polarization interaction terms, whereas $E^{\mathrm{vdw}}_{\mathrm{QM/MM}}$ accounts for non-covalent van der Waals interactions (i.e. Pauli repulsion and dispersion energies).

Polarizable QM/MM approaches differ from each other in the way they define $E^{\mathrm{ele}}_{\mathrm{QM/MM}}$ and $E^{\mathrm{pol}}_{\mathrm{QM/MM}}$. Generally, mutual polarization is achieved by assigning MM atoms with electrostatic quantities, which in the specific case of QM/FQ are the charges (q), whose value is not fixed but varies according to the *Electronegativity Equalization Principle* (EEP) [78], which states that, at equilibrium, all atoms of the system have the same instantaneous electronegativity. QM/FQFμ model is a pragmatical extension of QM/FQ that adds an induced dipole on each MM atom as an additional source of polarization, thus accounting for anisotropic interactions [60]. While QM/FQ is defined in terms of two atomic parameters, the electronegativity (χ) and the chemical hardness (η), in QM/FQFμ an additional parameter, i.e. the atomic polarizability (α), appears. Charges and dipoles are obtained by solving the following set of linear equations, which are derived from a variational minimization of the total energy of the system, under the constraint that the total charge of each solvent molecule is conserved [60]. To this end, a set of Lagrangian multipliers (λ) is exploited [60]:

$$\left(\begin{array}{ccc|c} \mathbf{T}^{\mathrm{qq}} & \mathbf{1}_{\lambda} & \mathbf{T}^{\mathrm{q}\mu} & \\ \mathbf{1}^{\dagger}_{\lambda} & \mathbf{0} & \mathbf{0} & \\ -\mathbf{T}^{\mathrm{q}\mu\,\dagger} & \mathbf{0} & \mathbf{T}^{\mu\mu} & \end{array}\right)\left(\begin{array}{c} \mathbf{q} \\ \lambda \\ \boldsymbol{\mu} \end{array}\right) = \left(\begin{array}{c} -\chi \\ \mathbf{Q}_{\mathrm{tot}} \\ \mathbf{0} \end{array}\right) + \left(\begin{array}{c} -\mathbf{V}(\rho) \\ \mathbf{0} \\ \mathbf{E}(\rho) \end{array}\right) \tag{3}$$

$$\Rightarrow \quad \mathbf{D}\mathbf{L}_{\lambda} = -\mathbf{C}_{Q} - \mathbf{R}(\rho)$$

In Eq. (3) $\mathbf{D}$ contains charge–charge $\mathbf{T}^{\mathrm{qq}}$, charge–dipole $\mathbf{T}^{\mathrm{q}\mu}$ and dipole–dipole $\mathbf{T}^{\mu\mu}$ interaction kernels. $\mathbf{L}$ collects charges $\mathbf{q}$, dipoles $\boldsymbol{\mu}$ and Lagrangian multipliers λ, whereas $\mathbf{C}_{Q}$ contains atomic electronegativities and the total charge of the system. $\mathbf{R}$ collects both the electrostatic potential and the field generated by the QM system at MM positions. Remarkably, both charges and dipoles are affected by the QM density and vice versa, thus accounting for mutual polarization. As a result, a non-linear term arises, which requires the QM/FQ(Fμ) linear system in Eq. (3) to be solved at each self-consistent field (SCF) cycle.

Raman and ROA scattering cross-sections for a vibrational transition from an electronic state i to a state j can be written in terms of geometrical derivatives of the following polarizability tensors [1]:

- electric dipole–dipole polarizability tensor

$$\alpha_{\alpha\beta} = \frac{1}{\hbar}\sum_{k\neq j,i}\left(\frac{\langle j|\hat{\mu}_{\alpha}|k\rangle\langle k|\hat{\mu}_{\beta}|i\rangle}{\omega_{ki}-\omega} + \frac{\langle j|\hat{\mu}_{\beta}|k\rangle\langle k|\hat{\mu}_{\alpha}|i\rangle}{\omega_{kj}+\omega}\right); \tag{4}$$

- electric dipole–magnetic dipole polarizability tensor

$$G'_{\alpha\beta} = \frac{1}{\hbar}\sum_{k\neq j,i}\left(\frac{\langle j|\hat{\mu}_\alpha|k\rangle\langle k|\hat{m}_\beta|i\rangle}{\omega_{ki}-\omega} + \frac{\langle j|\hat{m}_\beta|k\rangle\langle k|\hat{\mu}_\alpha|i\rangle}{\omega_{kj}+\omega}\right); \quad (5)$$

- electric dipole–electric quadrupole polarizability tensor

$$A_{\alpha\beta\gamma} = \frac{1}{\hbar}\sum_{k\neq j,i}\left(\frac{\langle j|\hat{\mu}_\alpha|k\rangle\langle k|\hat{\Theta}_{\beta\gamma}|i\rangle}{\omega_{ki}-\omega} + \frac{\langle j|\hat{\Theta}_{\beta\gamma}|k\rangle\langle k|\hat{\mu}_\alpha|i\rangle}{\omega_{kj}+\omega}\right). \quad (6)$$

In the previous equations, ω is the frequency of the external radiation and ω_{ki} is the frequency associated with the energy difference $\Delta E = \hbar\omega_{ki}$ between the initial and intermediate states involved in the transition. $\hat{\mu}$ is the electric dipole, $\hat{m}$ is the magnetic dipole and $\hat{\Theta}$ is the electric quadrupole operator. Raman scattering is only defined in terms of $\alpha_{\alpha\beta}$, whereas ROA arises from the combination of all three tensors defined above.

The tensors in Eqs. (4)–(6) can be calculated by exploiting Time-Dependent (TD)-DFT Linear Response Theory, formulated in terms of Coupled-Perturbed Kohn–Sham (CPKS) equations [25,62,79,80]. Raman and ROA signals are then computed by numerically differentiating the tensors with respect to normal modes. It is important to note that, in line with the paradigm of "focused" models, it is assumed that the geometrical perturbation only acts on the QM part of the system (the solute). Such a choice, which is consistent with the so-called *Partial Hessian Vibrational Approach* (PHVA) [81–83], implies that the considered normal modes only belong to the QM target, i.e. solvent vibrations are discarded.

3. Results

3.1. Computational details

The calculation of Raman and ROA spectra of molecular systems in aqueous solution is performed by exploiting the computational protocol explained in detail in Ref. [40]. It consists of the following five steps:

1. *Definition of the system*: Similarly to previous studies [40], we exploit a two-level partitioning, where the solute is treated at the QM level, while solvent molecules are modeled with an MM force-field.
2. *Classical MD simulations and sampling*: This step aims at obtaining a representative conformational sampling of the solvated system. MD simulations need to be long enough (generally tens of ns for aqueous solutions) to accurately sample the solute–solvent phase space and explore the solute's conformations [40]. Examples of explicitly solvated structures for the solutes analyzed in this work are included in Fig. S1 in the Supplementary Material (SM).
3. *Extraction of structures*: The analysis of MD runs in terms of hydration pattern is followed by the extraction of a number of uncorrelated structures. After such structures are cut into spheres of a given radius (large enough to include multiple solvation shells), they are employed in the subsequent Raman/ROA QM/FQ(Fμ) calculations.
4. *QM/FQ(Fμ) calculations*: For each spherical snapshot, the solute geometry is optimized at the QM/FQ(Fμ) level, while the solvent is kept frozen in order to preserve the sampling of the solvent configurational space obtained by classical MD. Such a procedure is in line with the philosophy of "focused" models. QM/FQ(Fμ) Raman and ROA spectra are then computed on those optimized structures.
5. *Analysis of the results*: Finally, computed QM/FQ(Fμ) signals for each spherical snapshot are averaged to produce spectra.

As a starting point of classical MD runs, SER and CYS (zwitterions, see Fig. 1a,d) lowest energy conformers are taken from the literature [76,84], optimized and vibrationally characterized as true minima at the B3LYP/TZP/COSMO level. CM5 atomic charges [85] are calculated at the same level of theory and further used in MD simulations, which are performed with the GROMACS package [86] and the GAFF force field [87]. Cubes of 5.5 nm length are used as solvation boxes and filled with a single solute molecule and about 5200 TIP3P water molecules [88]. The initial relaxation of the structures is done through energy minimization with the steepest descent minimization algorithm. Then, two equilibration steps are performed: first, an equilibration (1 ns) is conducted under the NVT ensemble in order to reach a temperature of 298 K with a velocity-rescaling method [89] and coupling constant of 0.1 ps. The equilibration of pressure (lasting 1 ns) is carried out under the NPT ensemble with pressure coupling with the Parrinello–Rahman barostat [90]. In the MD production stage, the system is let to evolve for 30 ns by using a leap-frog integration algorithm [91] with an integration time step of 2 fs. During production, the LINCS algorithm [92] is used to reset bonds to their correct length; electrostatic interactions are treated with the Particle Mesh Ewald method [93].

The last 20 ns of MD trajectories are used to extract 400 uncorrelated snapshots (one every 50 ps), which are subsequently cut in spherical shapes (radius = 17 Å) centered on the amino acid (~ 720 water molecules). Raman and ROA spectra on each spherical droplet (optimized as explained above at the B3LYP/TZP level) are computed by using the non-polarizable QM/TIP3P [94] and polarizable QM/FQ and QM/FQFμ approaches. QM/FQ and QM/FQFμ calculations employ the parametrization sets presented in Refs. [95] and [60], respectively. QM/continuum (COSMO [77]) spectra are also computed for the sake of comparison. In particular, for CYS, QM/COSMO spectra are obtained by using the five minimum conformations reported in Ref. [84]. For solvated SER, the most populated conformers as sampled during MD runs are considered. Such structures are determined through a clustering analysis [96] performed by exploiting the tools available in GROMACS. Importantly, a bi-dimensional scan of the main dihedrals of SER leads to the same lowest-energy conformers as found with the clustering methodology, as displayed in Fig. S2 in the SM. All QM/MM spectra are computed at the B3LYP/TZP level for the QM portion. Further spectral computations performed with an augmented basis set, namely B3LYP/ATZP, lead to changes in the relative intensities and the sign of some peaks in the ROA case, as shown in Fig. S3 in the SM for one of the snapshots. However, the computational cost increases more than 2.5 times, so it is very expensive for a large set of snapshots. Raman and ROA final spectra are obtained by averaging raw data and then by convoluting sticks with a Lorentzian line shape, with full width at half maximum (FWHM) equal to 6 cm^{-1}. All QM/MM and QM/COSMO calculations are performed by using a locally modified version of the ADF program package [97,98]. Polarizability derivatives involved in the definition of Raman and ROA intensities are performed by using numerical three-point differentiation with respect to Cartesian displacements (step = 0.05 Bohr) [99,100]. In all cases, the external frequency is set to 532 nm, according to experimental measurements [72,84].

3.2. Conformational analysis and hydration patterns of L-Serine and L-Cysteine

MD runs are first analyzed by performing a clustering analysis [96] (root-mean-square deviation (RMSD) threshold = 0.09 a.u.) so as to characterize SER and CYS main conformations. As a result, 5 and 6 conformers for SER and CYS, respectively, are identified (see Fig. 1c,f for the distribution of the two dihedral angles δ_1 and δ_2). To deeply analyze solute–solvent HB interactions, radial distribution functions *g(r)* (RDFs) are extracted from MD trajectories together with the running coordination number (RCN). RCN represents the number of closest water molecules interacting with the considered amino acid *via* HB. CYS carboxylic and amino groups RDFs are plotted in Fig. 1b. For the oxygen atoms of the carboxyl group and the hydrogen atoms of the amino group, a first solvation shell is identified at about 1.9 Å,

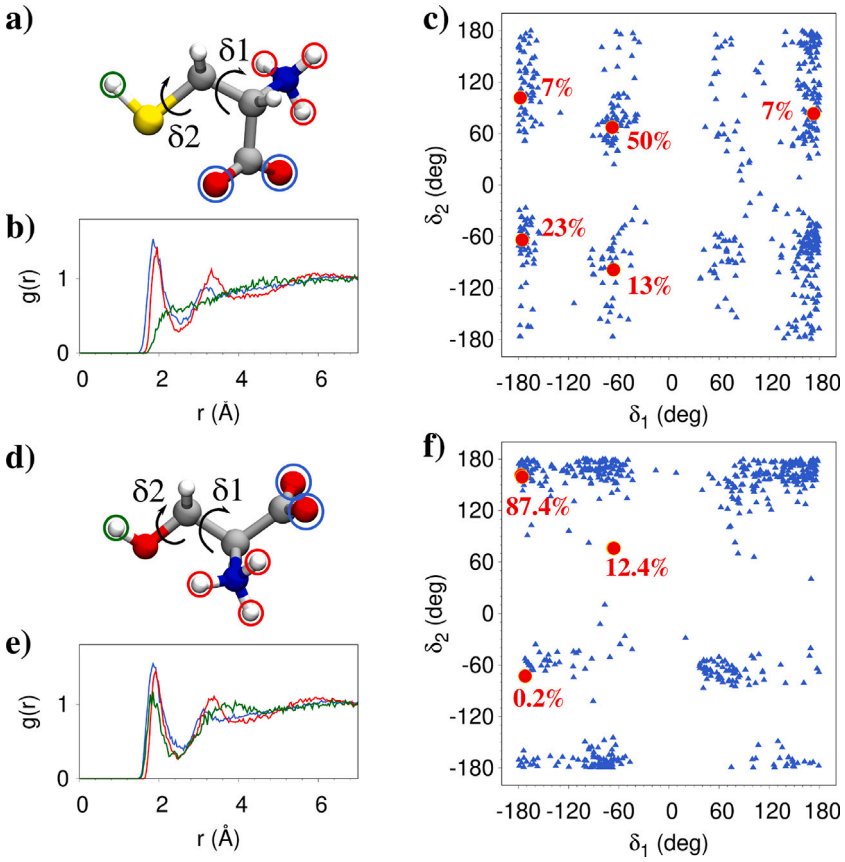

Fig. 1. (a) CYS molecular structure. (b) RDF for selected atoms of CYS (see panel a). (c) MD conformational analysis (blue triangles) for CYS in aqueous solution as a function of δ_1 and δ_2 (see panel a). QM/COSMO conformations, and their Boltzmann populations, are also reported as red circles. (d) SER molecular structure. (e) RDF for selected atoms of SER (see panel d). (f) MD conformational analysis (blue triangles) for SER in aqueous solution as a function of δ_1 and δ_2 (see panel d). QM/COSMO conformations, and their Boltzmann populations, are also reported as red circles.

associated with an RCN of almost 3 (for O) and 1 (for H). This indicates that the carboxylic group forms on average HBs with three water molecules, whereas the amino group is hydrogen bonded with a single solvent molecule. Moreover, no intermolecular HBs between H-(S) and water molecules, and intramolecular HBs between H (amino group) and O (carboxyl group) are detected. We note that these results are in accordance with previous studies reported in the literature [84].

A similar analysis can be performed on SER (see Fig. 1e), for which we consider the hydroxyl, carboxylic, and amino groups. RDFs of all these groups are characterized by an intense peak, centered at about 1.85 Å for the first shell of solvation, confirming the presence of HB interactions. The corresponding RCN is approximately 1 for hydrogen atoms and 3 for oxygen atoms. The obtained intermolecular HBs network of SER with the closest water molecules agrees with previous reports [76]. No intramolecular hydrogen bonds between the hydrogen atoms of the amino group and the oxygen atoms of the carboxylic group are observed.

The analysis of hydration patterns reveals that both systems are strongly interacting with water molecules via hydrogen bonding. Not unexpectedly, a different picture arises by exploiting a continuum solvation approach (QM/COSMO). We analyze the conformational distribution as a function of the two dihedral angles (δ_1 and δ_2, see Fig. 1a,d for their definition). QM/COSMO δ_1 and δ_2 values are reported in Fig. 1c,f (red points), together with the corresponding values computed on the 400 snapshots optimized at the QM/FQ level. The latter (see Fig. 1c for CYS) shows a huge variability of both δ_1 and δ_2 angles, which are clustered in about 5–6 regions. Indeed, a large region is sampled by QM/FQ but not by QM/COSMO (δ_1 between 50 to 100 degrees). Remarkably, the strong interaction with solvent molecules predicted from MD simulations makes the formation of intramolecular HBs unfavorable, thus the observed CYS conformers are all characterized by intermolecular interactions. Moving to SER (see Fig. 1f), three main QM/COSMO conformers are observed, whereas QM/FQ values explore a large region of space. As expected, the O–H group is highly dynamic in aqueous solution, due to the formation of HBs with solvent molecules (see rdf in Fig. 1e). Note that one of the QM/COSMO conformers is characterized by an intramolecular interaction between the carboxylic and hydroxyl groups ($\delta_1 \sim -60, \delta_2 \sim 70$), which is absent in atomistic simulations, for which intermolecular HBs are mainly established, as expected.

3.3. Raman and ROA spectra of L-Cysteine

On the basis of the conformational analysis reported in the previous section, here QM/COSMO and QM/MM Raman and ROA spectra of CYS in aqueous solution are analyzed. Calculated Raman and ROA stick spectra, i.e. the raw data extracted from each structure, are reported in Fig. 2. For QM/MM results, the selected number of snapshots (400) guarantees the convergence on averaged spectra (see also Fig. S4a in the SM).

Let us first focus on Raman spectra (see Fig. 2). QM/COSMO spectrum is characterized by three dominating peaks: two of them are placed in the region between 600 and 800 cm^{-1} and the third one between 1500 and 1600 cm^{-1}. The intense peak at about 685 cm^{-1} is assigned to the C–S bond stretching (see Fig. S5e in the SM), whereas the peak at around 800 cm^{-1} is related to CO_2^- wagging (see Fig. S5g in the SM). The third peak (1500–1600 cm^{-1}) is associated to NH_3^+ wagging and CH_2 bending (see Fig. S5s,t in the SM). By moving to QM/MM

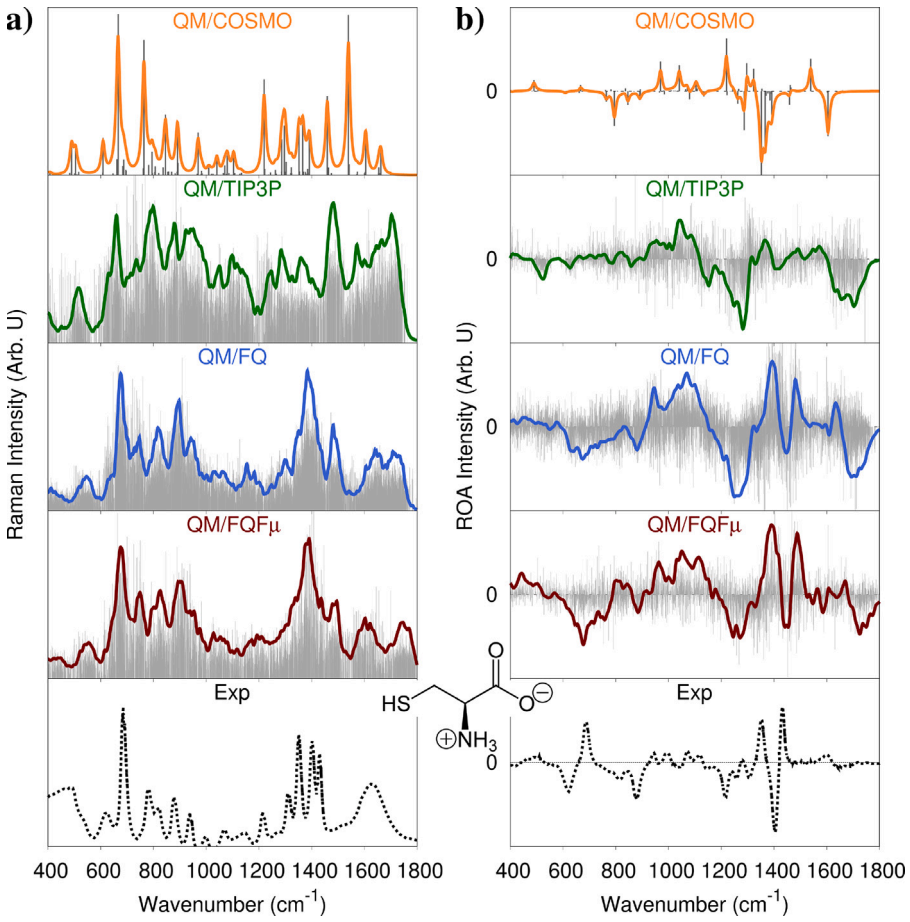

Fig. 2. QM/COSMO, QM/TIP3P, QM/FQ and QM/FQFμ Raman (a) and ROA (b) spectra of CYS in aqueous solution. Experimental Raman (a) and ROA (b) spectra, reproduced from Ref. [84], are also reported.

calculations, QM/TIP3P spectrum presents highly intense peaks in the region between 600 and 800 cm^{-1} (which are assigned similarly to QM/COSMO calculations) and between 1400 and 1500 cm^{-1}, associated to CH_2 and C–H bending modes (see Fig. S5r in the SM). Remarkably, QM/TIP3P and QM/COSMO spectra completely disagree, in particular in terms of peaks' relative intensities and band-broadening. These differences are a direct consequence of hydrogen bonding and a dynamic picture of solvation. Let us now move on to show the effects of solute–solvent mutual polarization. QM/FQ and QM/FQFμ spectra are characterized by an intense peak at about 700 cm^{-1} (see Fig. S5e in the SM), in the central region around 900 cm^{-1} (asym. stretching of C–C–C, S–H bending, C–N stretching, see Fig. S5h,i in the SM) and in the region around 1400 cm^{-1}, associated with C–H bending, sym. stretching of CO_2^- and bending/wagging of CH_2 (see Fig. S5p–r in the SM). Both polarizable embedding models provide similar Raman spectra, and the effect of the dipoles (in QM/FQFμ) is thus not so relevant. However, it is worth noting some discrepancies between QM/FQ and QM/FQFμ in both vibrational frequencies (see for instance the region between 1600–1800 cm^{-1}) and relative intensities (e.g. 850–950 cm^{-1}). In particular, for the band around 1600–1800 cm^{-1} higher vibrational energies are reported for QM/FQFμ. These modes are associated with the asym. C=O stretching of the carbonyl group (see Fig. S5u in the SM) which strongly interacts with 3 water molecules (see Fig. 1b), for which the two models are expected to differ. Remarkably, both QM/FQ and QM/FQFμ spectra are different from the spectra derived from QM/COSMO and QM/TIP3P approaches, thus highlighting the major role played by the atomistic description (with respect to QM/COSMO) and by the inclusion of solute–solvent mutual polarization effects (with respect to QM/TIP3P).

By moving to ROA, a huge sign alternation pattern is revealed, highlighting the intrinsic complexity of this kind of chiroptical spectroscopy. Indeed, the variability arises from both conformational changes in the solute geometry and the solvent distribution around it, as sampled from MD simulations. We remark that a diverse picture comes from continuum modeling, which provides a simplified vision of both spectra. At first glance, it is not possible to clearly identify the shape of convoluted spectra from QM/MM stick spectra (see solid lines in Fig. 2), while QM/COSMO raw data are directly connected with final spectra. Another consequence of the commented variability is inhomogeneous band broadening, which is automatically obtained in QM/MM convoluted spectra due to a dynamical sampling. On the contrary, for static models such as QM/COSMO, the bandwidth is intrinsically homogeneous.

We now move on to the comparison with experimental data, reproduced from Ref. [84] (see Fig. 2). Some major discrepancies between experimental spectra and QM/TIP3P Raman calculations are reported, both in terms of vibrational frequencies and intensities, that consequently exhibit the poorest agreement. The QM/COSMO Raman spectrum discreetly reproduces the frequencies of the experimental data but it is not very accurate in the relative intensities. Significant improvement is achieved by exploiting QM/FQ and QM/FQFμ. In a detailed view of Raman spectra, the region near 800 cm^{-1} (see Fig. S5f,g in the SM) is well reproduced by both polarizable approaches, whereas both QM/TIP3P and QM/COSMO relative intensities are less accurate. Furthermore, the region near 1400 cm^{-1} (see also Fig. S5p–s in the SM) is correctly described by QM/FQ and QM/FQFμ, even if peaks are not perfectly resolved, whereas QM/TIP3P and QM/COSMO spectra are not directly comparable with experimental values. The good agreement with the experiment provided by both QM/FQ and QM/FQFμ

highlights the importance of correctly taking into account solvation dynamics and specific solute–solvent HB interactions. Also, the almost perfect agreement with experimental spectra which is achieved by using polarizable methods demonstrates the crucial importance of including mutual solute–solvent polarization in modeling Raman spectra.

A more complex scenario arises from the analysis of ROA spectra (see Fig. 2b), which as stated above are associated with an additional sign alternation pattern as a function of the snapshot. By comparing computed spectra, we note serious discrepancies between continuum and explicit modeling, which not only concern bands' relative intensities and positions but, more importantly, the sign alternation pattern, which is proper for a given enantiomer. In fact, QM/COSMO ROA spectrum is dominated by an intense (+,−,+,−) pattern between 1200 and 1400 cm^{-1}, which is associated with the asym. stretching of C–C–N, the C–H bending, the CH_2 wagging/twisting and the CO_2^- symmetric stretching (see Fig. S5m–q in the SM). QM/TIP3P spectrum is mainly dominated by intense (+,−,+) signals between 1000 and 1400 cm^{-1} (see Fig. S5j–q in the SM) and by a broad negative band between 1600 and 1750 cm^{-1} (see Fig. S5u-w in the SM). QM/FQ and QM/FQFμ spectra are characterized by a broad positive band between 900 to 1200 cm^{-1} (see Fig. S5i-e in the SM), connected with backbone modes, C–C–C stretching, NH_3^+ rocking, S–H and C–H bending, C–C–N rocking and asymmetric stretching. In addition, both spectra reveal a broad intense negative band between 1200 and 1300 cm^{-1} (see Fig. S5m-o in the SM). Another relevant region is around 1300–1500 cm^{-1}, for which a (+,−,+) pattern is reported (see Fig. 2b). Although the main features of the ROA spectrum are similarly reproduced by QM/FQ and QM/FQFμ, slight differences between the two polarizable approaches are appreciable with regard to bands' relative intensities (e.g. 1000–1200 cm^{-1} and 1300–1500 cm^{-1} regions), and in the sign of the peak near 800 cm^{-1}, which is positive for QM/FQFμ and negative for QM/FQ. These regions, as previously discussed, are related to CH_2 and C–H vibrational modes and CO_2^- wagging. Therefore, they are highly sensitive to the external environment and the solvation model (see also QM/COSMO and QM/TIP3P spectra for a comparison). However, the sign alternation pattern is coherent between QM/FQ and QM/FQFμ (with the only exception of the aforementioned peak at around 800 cm^{-1}). Differently from Raman, QM/TIP3P ROA spectrum is similar to QM/FQ and QM/FQFμ, showing almost the same sign alternation pattern with the exception of the negative peak around 1200 cm^{-1} and the region between 1300–1500 cm^{-1}, which is almost absent in QM/TIP3P. Furthermore, it is worth remarking that the dissimilarities between atomistic and continuum solvent descriptions in describing band-broadening are enhanced in ROA spectra as compared to Raman. This is not surprising and is related to the intrinsic complexity of ROA, which finds its strengths in its sensitivity to solute conformations and interactions with the surrounding environment.

By still focusing on the comparison with experimental data [84], we notice that the experimental ROA spectrum is mainly characterized by a (−,+) pattern (600–700 cm^{-1}), a negative peak at around 900 cm^{-1} and three (+,−,+) intense bands around 1400 cm^{-1}. QM/FQ and QM/FQFμ spectra are able to accurately reproduce such features. In particular, bands' relative intensities, widths, and frequencies are well-reproduced. QM/TIP3P, and especially QM/COSMO are strongly inaccurate. In fact, the main (+,−,+) pattern (1400 cm^{-1}) is almost perfectly simulated by QM/FQ and QM/FQFμ, whereas such bands are almost absent in QM/TIP3P calculations, and the sign alternation is not reported by QM/COSMO. Differently from Raman, the inclusion of an additional polarization source in QM/FQFμ yields a better agreement with the experimental spectrum, in particular for the bands between 1200 and 1600 cm^{-1}. This is mainly due to different relative intensity patterns as compared to QM/FQ, which wrongly predicts the negative band between 1200–1300 cm^{-1} to be the most intense. All methods fail at reproducing the sign alteration pattern between 600 and 700 cm^{-1} which is positive in experimental spectra but negative in all computed spectra. These discrepancies might be associated with anharmonicity and also with the fact that such bands are associated with the C–S stretching, for which the exploited level of theory can be insufficient, due to computational challenges associated with the modeling of the sulfur atom [101].

3.4. Raman and ROA spectra of L-serine

Computed stick Raman and ROA spectra for SER are shown in Fig. 3a–b. Similarly to CYS, QM/MM calculations are performed on 400 structures so as to ensure convergence with respect to the number of snapshots (see Fig. S4b in the SM).

QM/COSMO Raman spectrum is characterized by homogeneous peaks, among which the most intense can be found at 820 and 1050 cm^{-1}. Both peaks are associated with skeletal vibrations, (C–C–N symmetric stretching and C–C–C(O) asymmetric stretching, see Fig. S6c,g in the SM). Moving to QM/MM approaches, QM/TIP3P Raman spectrum is dominated by two intense peaks in the same regions as QM/COSMO (with the same assignment) and by three broad bands between 1300–1500 cm^{-1} (C–H bending, CO_2^- symmetric stretching and CH_2 wagging, see Fig. S6m–p in the SM). The variability in QM/TIP3P sticks leads to broad and convoluted averaged peaks, thus diversifying this spectrum from QM/COSMO, especially with regard to intensities and bandwidths. QM/FQ and QM/FQFμ spectra are dominated by an intense peak above 800 cm^{-1} (see Fig. S6c in the SM) and by a very broad band centered at about 1400 cm^{-1} (see Fig. S6m–p in the SM). Both polarizable approaches give similar spectra, with only slight changes in relative intensities (e.g. at 1500 cm^{-1}). These findings highlight that, in this case, the effect of dipoles (i.e QM/FQFμ) is negligible. On the contrary, major discrepancies between QM/FQ(Fμ) and QM/TIP3P Raman spectra are noticed, mainly regarding bandwidths and relative intensities. In fact, for QM/TIP3P, the most intense signals fall between 1000 and 1100 cm^{-1}, and the region between 1300–1500 cm^{-1} completely disagrees with QM/FQ(Fμ) spectra. Such regions involve normal modes of the carboxylic and hydroxyl groups, which are strongly interacting with water molecules (see RDFs in Fig. 1e); thus, they are expected to be differently described by diverse solvation approaches.

By moving to the comparison with experimental measurements [72], good agreement between calculated QM/FQ and QM/FQFμ spectra and experimental data is observed, with an almost perfect reproduction of experimental frequencies, relative intensities, and bandwidths. More in detail: (*i*) band at about 800 cm^{-1} (CO_2^- wagging, see Fig. S6b in the SM): its relative intensity is correctly reproduced by QM/FQ and QM/FQFμ only, while it is almost absent in QM/PCM and QM/TIP3P spectra. (*ii*) 1000–1200 cm^{-1} region (see Fig. S6b,d in the SM): the experimental spectrum is characterized by a broad low-in-intensity convoluted band. This band is among the most intense in QM/TIP3P and QM/PCM calculations, whereas it is correctly described by QM/FQ and QM/FQFμ. (*iii*) 1300–1500 cm^{-1} region (see Fig. S3m–q in the SM): the experimental spectrum features three intense and well-resolved peaks. Overall, the relative intensity of this region is correctly reproduced by both QM/FQ and QM/FQFμ however, two bands are barely visible, probably because two peaks fuse into a broadband. QM/COSMO and QM/TIP3P fail to reproduce this spectral region. By considering the nature of normal modes involved in the three analyzed regions, and the fact that they all involve HB sites, our results clearly demonstrate once again the crucial role of solute–solvent specific interactions and the important role of mutual solute–solvent polarization effects.

We now analyze ROA spectra reported in Fig. 3. QM/COSMO yields two predominant positive peaks, located at about 900 cm^{-1} (C–C(O_2) symmetric stretching) and 1100 cm^{-1} (C–C–N asymmetric stretching, C–H bending, NH_3^+ rocking). In addition, the range 1300–1400 cm^{-1} (C–H and O–H bendings, CH_2 twisting, CO_2^- symmetric stretching and C–H bending) shows a (+,−,+,−) sign pattern. QM/TIP3P spectrum features four positive broad bands between 800 and 1200 cm^{-1}

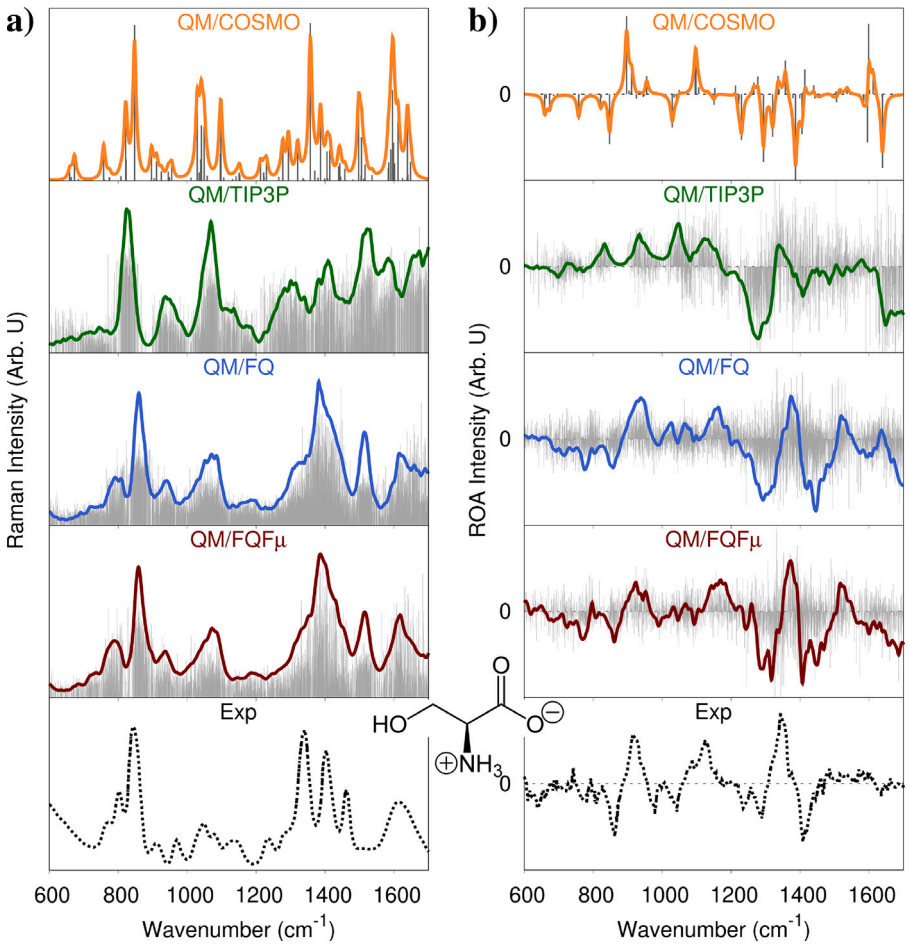

Fig. 3. QM/COSMO, QM/TIP3P, QM/FQ and QM/FQFμ Raman (a) and ROA (b) computed spectra of SER in aqueous solution. Experimental Raman (a) and ROA (b) spectra, reproduced from Ref. [72], are also reported.

and (−,+,−) sign alternation between 1250 and 1450 cm^{-1}. Overall, QM/TIP3P and QM/COSMO calculations disagree. QM/FQ and QM/FQFμ spectra are characterized by a clear (−,+,−) sign alternation pattern between 1250 and 1450 cm^{-1} and by a positive peak at 1500 cm^{-1} (see Fig. S6e–q in the SM). In addition, the QM/FQ spectrum features four positive peaks between 800 and 1200 cm^{-1} (see Fig. S6a–d in the SM), while the QM/FQFμ spectrum shows two dominant bands ($\sim$ 900 and $\sim$ 1110 cm^{-1}), and weak negative peaks between 1000 and 1100 cm^{-1}. In contrast to the Raman spectrum, and similarly to CYS, some discrepancies between QM/FQ and QM/FQFμ ROA spectra can be appreciated. This results from a higher sensitivity to the solvation description in the case of ROA than Raman. In fact, a different sign pattern is observed in particular at 800 cm^{-1} and between 1000 and 1100 cm^{-1}. Also, the band around 1300 cm^{-1} is better resolved in the QM/FQFμ spectrum. QM/FQ(Fμ), QM/TIP3P, and QM/COSMO predict largely different averaged ROA spectra. More specifically, the two central peaks between 950 and 1100 cm^{-1} are positive in the case of QM/TIP3P and QM/FQ, one positive and one negative for QM/COSMO and both negative in the case of QM/FQFμ. Because these peaks are related to O–H bending and backbone stretching models, mutual polarization effects and the explicit description of the solvent molecules significantly impact the final simulated spectra.

We finally move to the comparison with experimental data reported in Ref. [72]. The experimental spectrum is characterized by a (+,−,−,+) (900 and 1200 cm^{-1}) and an intense (+,−) sign alternation pattern between 1300 and 1450 cm^{-1}. QM/FQFμ accurately models ROA spectral features in terms of bandwidths, frequencies, and, most importantly, sign alternation (see for example the (−,+,−) pattern around 1400 cm^{-1}). However, relative intensities are less accurately reproduced for some bands. This is the case of the two negative peaks around 1000 cm^{-1}, which are weak in QM/FQFμ spectra. Also, the intensities of the two bands between 1200 and 1400 cm^{-1} and at 1500 cm^{-1} are overestimated. Apart from these slight discrepancies, the agreement between QM/FQFμ and experimental data is very good. QM/FQ and QM/TIP3P spectra are instead imprecise in the reproduction of the two peaks around 1000 cm^{-1} and the broad negative band between 1200 and 1300 cm^{-1}. Nevertheless, QM/FQ can correctly reproduce the main experimental features (for instance, the (−,+,−) pattern around 1400 cm^{-1}). QM/COSMO, as expected, badly matches with experiments, and fails at reproducing not only bandwidths but more importantly sign alternation patterns (see for instance the region 900–1100 cm^{-1} and that around 1400 cm^{-1}).

3.5. Is clustering reliable for the prediction of Raman and ROA spectra?

The clustering of MD trajectories is a very attractive practice that is often exploited in order to reduce the computational cost associated with QM/MM calculations, which generally require hundreds or even thousands of snapshots [52]. To investigate the performance of this approach in the calculation of Raman and ROA spectra in aqueous solution, in Fig. 4 we report CYS (panel a) and SER (panel b) QM/FQFμ spectra as computed as an average over 400 snapshots extracted from the MD (QM/FQFμ_{MD}, blue lines) and as a weighted average on the 5 and 6 representative structures obtained from the GROMOS clustering (QM/FQF$\mu_{clustering}$, red lines). Experimental spectra reproduced from Refs. [72,84] and are also depicted for the sake of comparison.

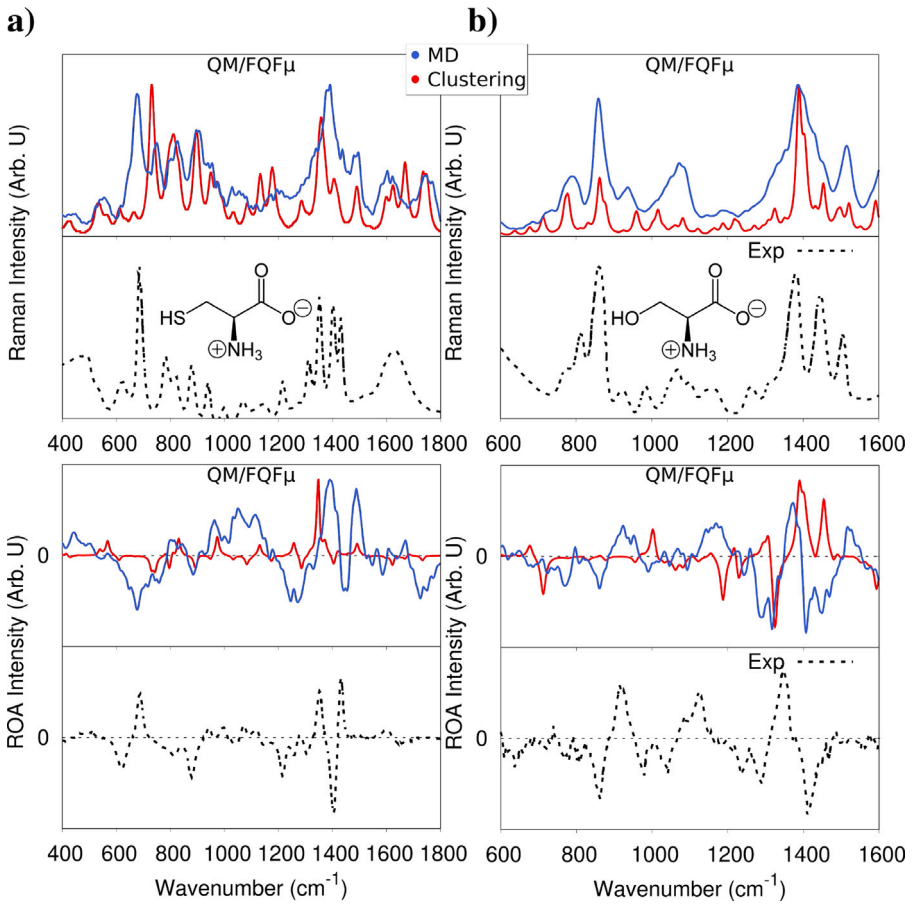

Fig. 4. QM/FQFμ_{MD} and QM/FQF$\mu_{clustering}$ Raman (top) and ROA (bottom) spectra of CYS (left) and SER (right) in aqueous solution. Experimental spectra are also reported [72,84].

By first focusing on Raman spectra, we notice for both CYS (panel a) and SER (panel b) that the main features of the spectrum are correctly reproduced by QM/FQF$\mu_{\text{clustering}}$. However, some discrepancies are present and mainly involve the position of the peaks, their relative intensities, and the inhomogeneous band broadening. This is not surprising, as the band inhomogeneity mostly arises from the many solvent configurations that are sampled during the MD. Such information is clearly lost in the clustering approach, which is based on the solute conformations only while neglecting the possible different orientations of the solvent molecules. The clustering and the neglecting of solvent orientation yield ROA spectra that largely diverge from QM/FQFμ_{MD}, even failing at reproducing their main features (e.g. the sign alternation in the region between 1300–1500 cm^{-1} for both molecules). This is due to the fact that QM/FQFμ_{MD} ROA spectra are obtained as an average over hundreds of snapshots characterized by a large variability of signs (see Figs. 2 and 3), while in a clustering vision, only a few structures are taken into consideration, potentially altering the sign pattern as in this case. Note that similar outcomes are obtained if QM/FQ is exploited (see Fig. S4 in the SM).

To consider the possible impact of a complete quantum treatment of the closest water molecules, we performed further calculations on the representative snapshots of CYS and SER explicitly including the water molecules belonging to the first solvation shell as extracted from the first minima in the RDFs. The results are added in Fig. S7 in the SM. The differences in the simulated spectra are mostly related to the relative intensities of the peaks for both systems and, in the ROA spectra, there are some changes in the signs of the peaks involving the groups that create hydrogen bond networks with the surrounding solvent molecules.

Our findings clearly show that spectral simulations on chiroptical properties performed on a few representative structures extracted from clustering procedures are generally inadequate to correctly reproduce the high complexity associated with chiroptical signals, for which solvent distribution plays indeed a fundamental role.

4. Summary and conclusions

We have presented the extension of QM/FQFμ to the calculation of Raman and ROA spectra. The approach is a pragmatical extension of QM/FQ, where mutual QM/MM polarization effects are refined by exploiting a set of fluctuating dipoles to take into account anisotropic interactions. To demonstrate the reliability and robustness of the method, it has been applied to the calculation of Raman and ROA spectra of (L)-cysteine and (L)-serine in aqueous solution. QM/FQFμ has also been compared to implicit QM/COSMO, non-polarizable QM/TIP3P, and polarizable QM/FQ approaches. The comparison takes into account various factors, including the way the solute–solvent phase space is sampled and the accuracy of the solvent description. In fact, SER and CYS exhibit high conformational flexibility and strong interactions with the surrounding water molecules. Implicit and explicit solvent descriptions provide a different picture of both Raman and ROA spectra in aqueous solution; as a consequence, they give a different description of spectra, and in this present case explicit, fully atomistic description yields a much better agreement with experiments than the continuum QM/COSMO approach.

Furthermore, the comparison between QM/TIP3P and polarizable QM/MM methods highlights the crucial role of solvent polarization in both Raman and ROA spectra. Indeed, for both CYS and SER, QM/FQ and QM/FQFμ models predict very similar Raman spectra, with only minor differences in relative intensities, thus showing that the inclusion of induced dipoles in QM/FQFμ does not particularly affect the final

spectra. For ROA spectra, both QM/FQ and QM/FQFμ approaches provide results that are in very good agreement with the experiment in terms of frequencies, intensities, and especially sign patterns. In particular, QM/FQFμ is able to improve the accuracy with respect to QM/FQ, thus highlighting the importance of including anisotropic solute–solvent interactions. Finally, the comparison of Raman and ROA spectra computed as an average over hundreds of snapshots extracted from MD simulations and over the representative clustered conformations of both SER and CYS highlights the necessity of correctly taking into account the solvent distribution around the solute.

To conclude, the developed methodology couples state-of-the-art polarizable QM/MM methods with a dynamical sampling obtained by means of classical MD simulations. For complex systems, characterized by several minima, more sophisticated methods, such as enhanced sampling, QM/MM or ab-initio dynamics might also be exploited [102, 103]. Furthermore, in polarizable QM/MM, solute–solvent interactions are limited to electrostatic (and polarization) contributions. Such an approximation can be justified for highly polar solvents, such as water, however non-electrostatic terms, such as Pauli repulsion and dispersion, might play a relevant role for apolar solvents. In the last years, we have developed a model to account for such contributions, general enough to be coupled to any QM/MM approach and to model any environment, pending a reliable parametrization [104]. Its extension to high-order properties and spectroscopies such as Raman and ROA is far from trivial, however, it is an interesting topic for future investigations. Also, the developed methodology can be applied to the simulation of Resonance Raman (RR) [54,105] and Resonance ROA (RROA) spectroscopies [106,107], for which the extension of the theoretical modeling to the evaluation of complex polarizabilities would be needed [108].

CRediT authorship contribution statement

Chiara Sepali: Methodology, Software, Formal analysis, Data curation, Investigation, Writing – original draft, Writing – review & editing. **Piero Lafiosca:** Methodology, Software, Validation, Data curation, Writing – original draft, Supervision, Writing – review & editing. **Sara Gómez:** Formal analysis, Investigation, Methodology, Writing – review & editing. **Tommaso Giovannini:** Conceptualization, Validation, Writing – original draft, Project administration, Writing – review & editing. **Chiara Cappelli:** Conceptualization, Resources, Funding acquisition, Project administration, Supervision, Writing – review & editing.

Declaration of competing interest

The authors declare that they have no known competing financial interests or personal relationships that could have appeared to influence the work reported in this paper.

Data availability

Data will be made available on request.

Acknowledgments

We gratefully acknowledge the Center for High Performance Computing (CHPC) at SNS for providing the computational infrastructure.

Appendix A. Supplementary data

Supplementary material related to this article can be found online at https://doi.org/10.1016/j.saa.2023.123485.

References

[1] L.A. Nafie, Vibrational Optical Activity: Principles and Applications, John Wiley & Sons, Chichester, 2011.
[2] J.R. Cheeseman, M.S. Shaik, P.L. Popelier, E.W. Blanch, Calculation of raman optical activity spectra of methyl-β-d-glucose incorporating a full molecular dynamics simulation of hydration effects, J. Am. Chem. Soc. 133 (13) (2011) 4991–4997.
[3] N. Berova, L. De Bari, G. Pescitelli, Application of electronic circular dichroism in configurational and conformational analysis of organic compounds, Chem. Soc. Rev. 36 (6) (2007) 914–931.
[4] L. Barron, A. Buckingham, Rayleigh and Raman scattering from optically active molecules, Mol. Phys. 20 (6) (1971) 1111–1119.
[5] P. Atkins, L. Barron, Rayleigh scattering of polarized photons by molecules, Mol. Phys. 16 (5) (1969) 453–466.
[6] L.D. Barron, L. Hecht, Vibrational Raman Optical Activity: From Fundamentals to Biochemical Applications, VCH, ISBN: 9781560816188, 1994, URL http://eprints.gla.ac.uk/138557/.
[7] L. Hecht, L.D. Barron, E.W. Blanch, A.F. Bell, L.A. Day, Raman optical activity instrument for studies of biopolymer structure and dynamics, J. Raman Spectrosc. 30 (9) (1999) 815–825.
[8] L. Barron, M. Bogaard, A. Buckingham, Raman scattering of circularly polarized light by optically active molecules, J. Am. Chem. Soc. 95 (2) (1973) 603–605.
[9] W. Hug, S. Kint, G.F. Bailey, J.R. Scherer, Raman circular intensity differential spectroscopy, spectra of (-)-. alpha.-pinene and (+)-. alpha.-phenylethylamine, J. Am. Chem. Soc. 97 (19) (1975) 5589–5590.
[10] F. Zhu, N.W. Isaacs, L. Hecht, L.D. Barron, Raman optical activity: A tool for protein structure analysis, Structure 13 (10) (2005) 1409–1419.
[11] Y. He, W. Bo, R.K. Dukor, L.A. Nafie, Determination of absolute configuration of chiral molecules using vibrational optical activity: A review, Appl. Spectrosc. 65 (7) (2011) 699–723.
[12] L.D. Barron, L. Hecht, I.H. McColl, E.W. Blanch, Raman optical activity comes of age, Mol. Phys. 102 (8) (2004) 731–744.
[13] L.D. Barron, The development of biomolecular raman optical activity spectroscopy, Biomed. Spectrosc. Imaging 4 (3) (2015) 223–253.
[14] P.L. Polavarapu, The absolute configuration of bromochlorofluoromethane, Angew. Chem., Int. Ed. 41 (23) (2002) 4544–4546.
[15] J. Haesler, I. Schindelholz, E. Riguet, C.G. Bochet, W. Hug, Absolute configuration of chirally deuterated neopentane, Nature 446 (7135) (2007) 526–529.
[16] J. Šebek J. Kapitán J. Sebestik, V. Baumruk, P. Bour, L-alanyl-l-alanine conformational changes induced by ph as monitored by the raman optical activity spectra, J. Phys. Chem. 113 (27) (2009) 7760–7768.
[17] L.A. Nafie, Vibrational optical activity: From discovery and development to future challenges, Chirality 32 (5) (2020) 667–692.
[18] L.A. Nafie, R.K. Dukor, Chapter 5 - vibrational optical activity in chiral analysis, in: P.L. Polavarapu (Ed.), Chiral Analysis, second ed., Elsevier, ISBN: 978-0-444-64027-7, 2018, pp. 201–247, http://dx.doi.org/10.1016/B978-0-444-64027-7.00005-7, URL https://www.sciencedirect.com/science/article/pii/B9780444640277000057.
[19] A. Rüther A. Forget, A. Roy, C. Carballo, R.K. Mießmer F. Dukor, L.A. Nafie, C. Johannessen, V.P. Shastri, S. Lüdeke, Unravelling a direct role for polysaccharide β-strands in the higher order structure of physical hydrogels, Angew. Chem. Int. Ed. 129 (16) (2017) 4674–4678.
[20] P.L. Polavarapu, Renaissance in chiroptical spectroscopic methods for molecular structure determination, Chem. Rec. 7 (2) (2007) 125–136.
[21] E.W. Blanch, L. Hecht, L.D. Barron, Vibrational Raman optical activity of proteins, nucleic acids, and viruses, Methods 29 (2) (2003) 196–209.
[22] F. Zhu, G.E. Tranter, N.W. Isaacs, L. Hecht, L.D. Barron, Delineation of protein structure classes from multivariate analysis of protein Raman optical activity data, J. Mol. Biol. 363 (1) (2006) 19–26.
[23] L. Barron, L. Hecht, E. Blanch, A. Bell, Solution structure and dynamics of biomolecules from Raman optical activity, Prog. Biophys. Mol. Biol. 73 (1) (2000) 1–49.
[24] T. Giovannini, G. Del Frate, P. Lafiosca, C. Cappelli, Effective computational route towards vibrational optical activity spectra of chiral molecules in aqueous solution, Phys. Chem. Chem. Phys. 20 (2018) 9181–9197.
[25] T. Giovannini, F. Egidi, C. Cappelli, Theory and algorithms for chiroptical properties and spectroscopies of aqueous systems, Phys. Chem. Chem. Phys. 22 (2020) 22864–22879.
[26] T. Giovannini, M. Olszòwka, F. Egidi, J.R. Cheeseman, G. Scalmani, C. Cappelli, Polarizable embedding approach for the analytical calculation of Raman and Raman optical activity spectra of solvated systems, J. Chem. Theory. Comput. 13 (9) (2017) 4421–4435.
[27] M. Pecul, E. Lamparska, C. Cappelli, L. Frediani, K. Ruud, Solvent effects on Raman optical activity spectra calculated using the polarizable continuum model, J. Phys. Chem. A 110 (8) (2006) 2807–2815.
[28] B. Mennucci, C. Cappelli, R. Cammi, J. Tomasi, Modeling solvent effects on chiroptical properties, Chirality 23 (9) (2011) 717–729, http://dx.doi.org/10.1002/chir.20984.

[29] C. Cappelli, Integrated qm/polarizable mm/continuum approaches to model chiroptical properties of strongly interacting solute-solvent systems, Int. J. Quantum Chem. 116 (21) (2016) 1532–1542.

[30] P. Stephens, F. Devlin, C. Chabalowski, M.J. Frisch, Ab initio calculation of vibrational absorption and circular dichroism spectra using density functional force fields, J. Phys. Chem. 98 (45) (1994) 11623–11627.

[31] M. Pecul, New applications and challenges for computational roa spectroscopy, Chirality 21 (1E) (2009) E98–E104.

[32] C. Cappelli, S. Corni, J. Tomasi, Electronic and vibrational dynamic solvent effects on Raman spectra, J. Chem. Phys. 115 (12) (2001) 5531–5535.

[33] F. Lipparini, F. Egidi, C. Cappelli, V. Barone, The optical rotation of methyloxirane in aqueous solution: A never ending story? J. Chem. Theory Comput. 9 (4) (2013) 1880–1884.

[34] T. Giovannini, C. Cappelli, Continuum vs. atomistic approaches to computational spectroscopy of solvated systems, Chem. Commun. 59 (38) (2023) 5644–5660.

[35] A. Warshel, M. Karplus, Calculation of ground and excited state potential surfaces of conjugated molecules. I. Formulation and parametrization, J. Am. Chem. Soc. 94 (16) (1972) 5612–5625.

[36] A. Warshel, M. Levitt, Theoretical studies of enzymic reactions: Dielectric, electrostatic and steric stabilization of the carbonium ion in the reaction of lysozyme, J. Mol. Biol. 103 (2) (1976) 227–249.

[37] H. Lin, D. Truhlar, Qm/mm: what have we learned, where are we, and where do we go from here? Theor. Chem. Acc. 117 (2007) 185–199, http://dx.doi.org/10.1007/s00214-006-0143-z.

[38] H.M. Senn, W. Thiel, Qm/mm methods for biomolecular systems, Angew. Chem. Int. Ed. 48 (7) (2009) 1198–1229.

[39] K.H. Hopmann, K. Ruud, M. Pecul, A. Kudelski, M. Dračínský, P. Bour, Explicit versus implicit solvent modeling of Raman optical activity spectra, J. Phys. Chem. B 115 (14) (2011) 4128–4137.

[40] T. Giovannini, F. Egidi, C. Cappelli, Molecular spectroscopy of aqueous solutions: A theoretical perspective, Chem. Soc. Rev. 49 (16) (2020) 5664–5677.

[41] J. Tomasi, B. Mennucci, R. Cammi, Quantum mechanical continuum solvation models, Chem. Rev. 105 (8) (2005) 2999–3094.

[42] A.H. Steindal, K. Ruud, L. Frediani, K. Aidas, J. Kongsted, Excitation energies in solution: The fully polarizable qm/mm/pcm method, J. Phys. Chem. B 115 (12) (2011) 3027–3037.

[43] E. Boulanger, W. Thiel, Solvent boundary potentials for hybrid qm/mm computations using classical drude oscillators: A fully polarizable model, J. Chem. Theory Comput. 8 (11) (2012) 4527–4538.

[44] S. Gomez, T. Giovannini, C. Cappelli, Multiple facets of modeling electronic absorption spectra of systems in solution, ACS Phys. Chem. Au (2022) http://dx.doi.org/10.1021/acsphyschemau.2c00050.

[45] S.W. Rick, S.J. Stuart, B.J. Berne, Dynamical fluctuating charge force fields: Application to liquid water, J. Chem. Phys. 101 (7) (1994) 6141–6156.

[46] S.W. Rick, S.J. Stuart, J.S. Bader, B. Berne, Fluctuating charge force fields for aqueous solutions, J. Mol. Liq. 65 (1995) 31–40.

[47] S.J. Stuart, B. Berne, Effects of polarizability on the hydration of the chloride ion, J. Phys. Chem. 100 (29) (1996) 11934–11943.

[48] F. Egidi, R. Russo, I. Carnimeo, A. D'Urso, G. Mancini, C. Cappelli, The electronic circular dichroism of nicotine in aqueous solution: A test case for continuum and mixed explicit-continuum solvation approaches, J. Phys. Chem. A 119 (21) (2015) 5396–5404.

[49] I. Carnimeo, C. Cappelli, V. Barone, Analytical gradients for mp2, double hybrid functionals, and td-dft with polarizable embedding described by fluctuating charges, J Comput Chem 36 (31) (2015) 2271–2290.

[50] T. Giovannini, M. Olszowka, C. Cappelli, Effective fully polarizable qm/mm approach to model vibrational circular dichroism spectra of systems in aqueous solution, J. Chem. Theory Comput. 12 (11) (2016) 5483–5492.

[51] R. Di Remigio, T. Giovannini, M. Ambrosetti, C. Cappelli, L. Frediani, Fully polarizable qm/fluctuating charge approach to two-photon absorption of aqueous solutions, J. Chem. Theory Comput. 15 (7) (2019) 4056–4068.

[52] F. Egidi, T. Giovannini, G. Del Frate, P.M. Lemler, P.H. Vaccaro, C. Cappelli, A combined experimental and theoretical study of optical rotatory dispersion for (r)-glycidyl methyl ether in aqueous solution, Phys. Chem. Chem. Phys. 21 (7) (2019) 3644–3655.

[53] T. Gómez S. Giovannini, C. Cappelli, Absorption spectra of xanthines in aqueous solution: A computational study, Phys. Chem. Chem. Phys. 22 (10) (2020) 5929–5941.

[54] S. Gómez, F. Egidi, A. Puglisi, T. Giovannini, B. Rossi, C. Cappelli, Unlocking the power of resonance Raman spectroscopy: The case of amides in aqueous solution, J. Mol. Liq. 346 (2022) 117841.

[55] S. Skoko, C. Micheletti, E. Grifoni, F. Egidi, T. Giovannini, A. Pucci, C. Cappelli, Towards a cost-effective modeling of fluorescence in the condensed phase, Dyes Pigm. 215 (2023) 111227.

[56] L. Uribe, S. Gomez, F. Egidi, T. Giovannini, A. Restrepo, Computational hints for the simultaneous spectroscopic detection of common contaminants in water, J. Mol. Liq. 355 (2022) 118908.

[57] P. Lafiosca, T. Gómez S. Giovannini, C. Cappelli, Absorption properties of large complex molecular systems: The dftb/fluctuating charge approach, J. Chem. Theory Comput. 18 (3) (2022) 1765–1779.

[58] M. Ambrosetti, S. Skoko, T. Giovannini, C. Cappelli, Quantum mechanics/fluctuating charge protocol to compute solvatochromic shifts, J. Chem. Theory Comput. 17 (11) (2021) 7146–7156.

[59] L. Goletto, S. Gómez, J.H. Andersen, H. Koch, T. Giovannini, Linear response properties of solvated systems: A computational study, Phys. Chem. Chem. Phys. 24 (45) (2022) 27866–27878.

[60] T. Giovannini, A. Puglisi, M. Ambrosetti, C. Cappelli, Polarizable qm/mm approach with fluctuating charges and fluctuating dipoles: The qm/fq$f\mu$ model, J. Chem. Theory Comput. 15 (2019) 2233–2245.

[61] T. Giovannini, R.R. Riso, M. Ambrosetti, A. Puglisi, C. Cappelli, Electronic transitions for a fully polarizable qm/mm approach based on fluctuating charges and fluctuating dipoles: Linear and corrected linear response regimes, J. Chem. Phys. 151 (17) (2019) 174104.

[62] T. Giovannini, L. Grazioli, M. Ambrosetti, C. Cappelli, Calculation of ir spectra with a fully polarizable qm/mm approach based on fluctuating charges and fluctuating dipoles, J. Chem. Theory Comput. 15 (10) (2019) 5495–5507.

[63] C. Mensch, P. Bultinck, C. Johannessen, The effect of protein backbone hydration on the amide vibrations in Raman and Raman optical activity spectra, Phys. Chem. Chem. Phys. 21 (4) (2019) 1988–2005.

[64] C. Cantor, P. Schimmel, Biophysical Chemistry: Part II: Techniques for the Study of Biological Structure and Function. Biophysical Chemistry, W. H. Freeman, ISBN: 9780716711902, 1980, URL https://books.google.it/books?id=l5XXRhNMjOMC.

[65] T.H. Jukes, Indications of an evolutionary pathway in the amino acid code, Biochem. Biophys. Res. Commun. 27 (5) (1967) 573–578.

[66] J.L. Bada, D.P. Glavin, G.D. McDonald, L. Becker, A search for endogenous amino acids in martian meteorite alh84001, Science 279 (5349) (1998) 362–365.

[67] T.K. Kim, M.S. Jhon, Theoretical study on the water structure of the aqueous amino acid solutions using Monte carlo method, J. Mol. Liq. 59 (2–3) (1994) 179–194.

[68] L. Stryer, J. Berg, J. Tymoczko, Bioquímica. 7a Edición: Con Aplicaciones Clínicas, Reverte, ISBN: 9788429194128, 2018, URL https://books.google.it/books?id=LLHfDwAAQBAJ.

[69] G. Schulz, R. Schirmer, Principles of Protein Structure. Springer Advanced Texts in Chemistry, Springer New York, ISBN: 9781461261377, 2013, URL https://books.google.it/books?id=FPLjBwAAQBAJ.

[70] M. Pecul, Theoretical simulation of the roa spectra of neutral cysteine and serine, Chem. Phys. Lett. 427 (1–3) (2006) 166–176.

[71] M. Osińska K. Pecul, A. Kudelski, Circularly polarized component in surface-enhanced Raman spectra, Chem. Phys. Lett. 496 (1–3) (2010) 86–90.

[72] A. Gargaro, L. Barron, L. Hecht, Vibrational Raman optical activity of simple amino acids, J. Raman. Spectrosc. 24 (2) (1993) 91–96.

[73] J. Sadlej, J.C. Dobrowolski, J.E. Rode, M.H. Jamróz, Density functional theory study on vibrational circular dichroism as a tool for analysis of intermolecular systems:(1: 1) cysteine- water complex conformations, J. Phys. Chem. A 111 (42) (2007) 10703–10711.

[74] M. Graff, J. Bukowska, Adsorption of enantiomeric and racemic cysteine on a silver electrode- sers sensitivity to chirality of adsorbed molecules, J. Phys. Chem. B 109 (19) (2005) 9567–9574.

[75] B. Hernández, F. Pflüger, A. Adenier, M. Nsangou, S.G. Kruglik, M. Ghomi, Energy maps, side chain conformational flexibility, and vibrational features of polar amino acids l-serine and l-threonine in aqueous environment, J. Chem. Phys. 135 (5) (2011) 08B601.

[76] P. Zhu, G. Yang, M.R. Poopari, Z. Bie, Y. Xu, Conformations of serine in aqueous solutions as revealed by vibrational circular dichroism, ChemPhysChem 13 (5) (2012) 1272–1281.

[77] A. Klamt, G. Schüürmann, Cosmo: A new approach to dielectric screening in solvents with explicit expressions for the screening energy and its gradient, J. Chem. Soc., Perkin Trans. II 2 (1993) 799–805.

[78] R. Sanderson, An interpretation of bond lengths and a classification of bonds, Science 114 (2973) (1951) 670–672.

[79] M.E. Casida, Time-dependent density functional response theory for molecules, in: Recent Advances in Density Functional Methods, World Scientific, 1995, pp. 155–192.

[80] P. Lafiosca, L. Nicoli, L. Bonatti, T. Giovannini, S. Corni, C. Cappelli, Qm/classical modeling of surface enhanced Raman scattering based on atomistic electromagnetic models, J. Chem. Theory Comput. (2023) http://dx.doi.org/10.1021/acs.jctc.3c00177.

[81] S. Jin, J.D. Head, Theoretical investigation of molecular water adsorption on the Al (111) surface, Surf. Sci. 318 (1–2) (1994) 204–216.

[82] M.D. Calvin, J.D. Head, S. Jin, Theoretically modelling the water bilayer on the Al (111) surface using cluster calculations, Surf. Sci. 345 (1–2) (1996) 161–172.

[83] A. Biancardi, R. Cammi, C. Cappelli, B. Mennucci, J. Tomasi, Modelling vibrational coupling in dna oligomers: A computational strategy combining qm and continuum solvation models, Theor. Chem. Acc. 131 (3) (2012) 1–10.

[84] M. Kaminski, A. Kudelski, M. Pecul, Vibrational optical activity of cysteine in aqueous solution: A comparison of theoretical and experimental spectra, J. Phys. Chem. B 116 (16) (2012) 4976–4990.

[85] A.V. Marenich, S.V. Jerome, C.J. Cramer, D.G. Truhlar, Charge model 5: An extension of hirshfeld population analysis for the accurate description of molecular interactions in gaseous and condensed phases, J. Chem. Theory Comput. 8 (2) (2012) 527–541, http://dx.doi.org/10.1021/ct200866d.

[86] M.J. Abrahama, T. Murtola, R. Schulz, J.C. Pálla S. Smith, B. Hess, E. Lindahl, GROMACS: High performance molecular simulations through multi-level parallelism from laptops to supercomputers, SoftwareX 1-2 (2015) 19–25.

[87] J. Wang, R.M. Wolf, J.W. Caldwell, P.A. Kollman, D.A. Case, Development and testing of a general amber force field, J. Comput. Chem. 25 (9) (2004) 1157–1174, http://dx.doi.org/10.1002/jcc.20035, URL https://onlinelibrary.wiley.com/doi/abs/10.1002/jcc.20035.

[88] P. Mark, L. Nilsson, Structure and dynamics of the TIP3P, SPC, and SPC/E water models at 298 K, J. Phys. Chem. A 105 (43) (2001) 9954–9960.

[89] G. Bussi, D. Donadio, M. Parrinello, Canonical sampling through velocity rescaling, J. Chem. Phys. 126 (1) (2007) 014101, http://dx.doi.org/10.1063/1.2408420.

[90] M. Parrinello, A. Rahman, Strain fluctuations and elastic constants, J. Chem. Phys. 76 (5) (1982) 2662–2666, http://dx.doi.org/10.1063/1.443248.

[91] G. Ciccotti, S. italiana di fisica, Molecular - dynamics simulation of statistical - mechanical systems, in: Proceedings of the International School of Physics "Enrico Fermi", North-Holland, ISBN: 9780444370334, 1986, URL https://books.google.it/books?id=lXHZjgEACAAJ.

[92] B. Hess, H. Bekker, H.J.C. Berendsen, J.G.E.M. Fraaije, Lincs: A linear constraint solver for molecular simulations, J Comput Chem 18 (12) (1997) 1463–1472, http://dx.doi.org/10.1002/(SICI)1096-987X(199709)18:12<1463::AID-JCC4>3.0.CO;2-H, URL https://onlinelibrary.wiley.com/doi/abs/10.1002/%28SICI%291096-987X%28199709%2918%3A12%3C1463%3A%3AAID-JCC4%3E3.0.CO%3B2-H.

[93] T. Darden, D. York, L. Pedersen, Particle mesh ewald: An nlog(n) method for ewald sums in large systems, J. Chem. Phys. 98 (12) (1993) 10089–10092, http://dx.doi.org/10.1063/1.464397.

[94] W.L. Jorgensen, Quantum and statistical mechanical studies of liquids. 10. Transferable intermolecular potential functions for water, alcohols, and ethers. Application to liquid water, J. Am. Chem. Soc. 103 (2) (1981) 335–340.

[95] S.W. Rick, S.J. Stuart, B.J. Berne, Dynamical fluctuating charge force fields: Application to liquid water, J Chem Phys 101 (7) (1994) 6141–6156.

[96] X. Daura, K. Gademann, B. Jaun, D. Seebach, W.F. van Gunsteren, A.E. Mark, Peptide folding: When simulation meets experiment, Angew. Chem., Int. Ed. 38 (1–2) (1999) 236–240.

[97] E. Baerends, P. Ros, Evaluation of the lcao hartree–fock–slater method: Applications to transition-metal complexes, Int. J. Quantum Chem. 14 (S12) (1978) 169–190.

[98] E. Baerends, et al., Adf (Version 2019.403), Software for Chemistry & Materials, Scm, 2019, URL http://www.scm.com. Theoretical Chemistry, Vrije Universiteit, Amsterdam, The Netherlands.

[99] L. Jensen, J. Autschbach, M. Krykunov, G. Schatz, Resonance vibrational Raman optical activity: A time-dependent density functional theory approach, J. Chem. Phys. 127 (13) (2007) 134101.

[100] M. Reiher, J. Neugebauer, B.A. Hess, Quantum chemical calculation of Raman intensities for large molecules: The photoisomerization of [{Fe 'S4' (PR3)} 2 (n2h2)]('s4' 2-=1, 2-bis (2-mercaptophenylthio)-ethane (2-)), Z. Phys. Chem. 217 (2) (2003) 91–104.

[101] E. Penocchio, M. Mendolicchio, N. Tasinato, V. Barone, Structural features of the carbon–sulfur chemical bond: A semi-experimental perspective, Can. J. Chem. 94 (12) (2016) 1065–1076.

[102] A. Laio, M. Parrinello, Escaping free-energy minima, P. Natl. Acad. Sci. 99 (20) (2002) 12562–12566.

[103] A. Laio, F.L. Gervasio, Metadynamics: A method to simulate rare events and reconstruct the free energy in biophysics, chemistry and material science, Rep. Prog. Phys. 71 (12) (2008) 126601.

[104] T. Giovannini, P. Lafiosca, C. Cappelli, A general route to include pauli repulsion and quantum dispersion effects in qm/mm approaches, J. Chem. Theory Comput. 13 (10) (2017) 4854–4870.

[105] P. Gómez S. Lafiosca, F. Egidi, T. Giovannini, C. Cappelli, Uv-resonance Raman spectra of systems in complex environments: A multiscale modeling applied to doxorubicin intercalated into dna, J. Chem. Info. Model 63 (4) (2023) 1208–1217.

[106] L.N. Vidal, F. Egidi, V. Barone, C. Cappelli, Origin invariance in vibrational resonance Raman optical activity, J. Chem. Phys. 142 (2015) 174101.

[107] L.N. Vidal, T. Giovannini, C. Cappelli, Can the resonance Raman optical activity spectrum display sign alternation? J. Phys. Chem. Lett. 7 (18) (2016) 3585–3590.

[108] L. Jensen, G.C. Schatz, Resonance Raman scattering of rhodamine 6g as calculated using time-dependent density functional theory, J. Phys. Chem. A 110 (18) (2006) 5973–5977.